$NiRh_2O_4$: A spin-orbit entangled diamond-lattice paramagnet

Shreya Das,[1] Dhani Nafday,[2] Tanusri Saha-Dasgupta,[1,2] and Arun Paramekanti[3,*]
[1]*Department of Condensed Matter Physics and Materials Science, S.N. Bose National Centre for Basic Sciences, Kolkata 700098, India*
[2]*School of Mathematical and Computational Sciences, Indian Association for the Cultivation of Science, Kolkata 700 032, India*
[3]*Department of Physics, University of Toronto, Toronto, Ontario, Canada M5S 1A7*

Motivated by the interest in topological quantum paramagnets in candidate spin-1 magnets, we investigate the diamond-lattice compound $NiRh_2O_4$ using *ab initio* theory and model Hamiltonian approaches. Our density functional study, taking into account the unquenched orbital degrees of freedom, shows stabilization of $S = 1$, $L = 1$ state. We highlight the importance of spin-orbit coupling, in addition to Coulomb correlations, in driving the insulating gap, and uncover frustrating large second-neighbor exchange mediated by Ni-Rh covalency. A single-site model Hamiltonian incorporating the large tetragonal distortion is shown to give rise to a spin-orbit entangled nonmagnetic ground state, largely accounting for the entropy, magnetic susceptibility, and inelastic neutron scattering results. Incorporating intersite exchange within a slave-boson theory, we show that exchange frustration can suppress exciton condensation. We capture the dispersive gapped magnetic modes, uncover "dark states" invisible to neutrons, and make predictions.

Introduction. Symmetry protected topological (SPT) phases of quantum matter such as two-dimensional (2D) and three-dimensional (3D) topological insulators [1,2], Weyl semimetals [3], and topological superconductors [2], have been found in electronic systems. Following these discoveries, interacting spins and bosons have also been proposed to support SPT phases with conventional bulk excitations but unconventional gapless or gapped edge states [4–8].

Recently, there has been an exciting suggestion that certain $S = 1$ spin models on the diamond lattice may realize a time-reversal symmetry protected topological quantum paramagnet [9], a 3D analog of the Haldane chain [10,11], with gapless 2D surface states. This has led to a renewed interest in candidate spinel materials AB_2O_4 with A-site spins on the diamond lattice. Studies of $MnSc_2S_4$ ($S = 5/2$), $CoAl_2O_4$ and $CoRh_2O_4$ ($S = 3/2$), and $CuRh_2O_4$ ($S = 1/2$) reveal spin spiral or helix or Néel orders [12–18]. On the other hand, $FeSc_2S_4$ shows very weak Néel order in proximity to a nonmagnetic ground state induced by spin-orbit coupling (SOC) [19–21], although excess Fe might play a role in nucleating Néel order [22]. The search for $S = 1$ topological paramagnets recently led to an intense investigation of $NiRh_2O_4$ [23].

$NiRh_2O_4$ is an unusual example of spin-1 $3d$ ions on the tetrahedrally coordinated A site, structurally stabilized by placing a $4d$ Rh^{3+} ion at the octahedral B site. While $NiRh_2O_4$ is cubic at high temperature [23,24], it transforms into a tetragonal phase below $T \sim 440$ K. Remarkably, in contrast to expectations from a Jahn-Teller mechanism which would favor $c/a < 1$ and an $S = 1$ ground state with quenched orbital angular momentum, the tetragonal phase is found to be elongated with $c/a \approx 1.05$. Such a tetragonal distortion, with $c/a > 1$, leaves the t_2 states of Ni partially filled. The active orbital degrees of freedom allows SOC to play an important role. The mechanism for tetragonal distortion must rely on SOC-induced orbital ordering, as discussed [25,26] in the B-site active spinel ZnV_2O_4. Upon cooling, $NiRh_2O_4$ displays a Schottky anomaly in the specific heat at $T \sim 30$–40 K, and spin gapped excitations in inelastic neutron scattering (INS).

$NiRh_2O_4$ was argued [23] to exhibit characteristics of valence bond solids or topological paramagnets, but an alternate crystal field level scheme was also proposed with a nonmagnetic ground state [27]. A theoretical study [28] of $NiRh_2O_4$ considered a frustrated Heisenberg model with antiferromagnetic (AFM) first- and second-neighbor exchanges (J_1 and J_2), and proposed that a nonmagnetic ground state might arise from large single-ion anisotropy DS_z^2, with $D > 0$ favoring local $S_z = 0$. A pseudofermion functional renormalization group study of the J_1-J_2 model [29] found that while the $S = 1$ case favors a quantum spiral spin liquid, tetragonal distortion or large $D/J_1 \gtrsim 8$ respectively favor Néel order or the $S_z = 0$ ground state. Both studies ignored orbital degrees of freedom. Recently, SOC in a tetrahedral crystal field was argued to support a $J_{\rm eff} = 0$ state at d^8 filling [30], similar to $J_{\rm eff} = 0$ insulators for d^4 filling in an octahedral environment [31–33]; however, for Ni^{2+}, this may be overwhelmed by distortions given its weak SOC. The INS results [23] on $NiRh_2O_4$ also remain to be understood; previous work used spin-wave theory assuming AFM order [23] while recognizing this was not appropriate. A proper and consistent theory of $NiRh_2O_4$ is thus still lacking. Here, we combine first-principles density functional theory (DFT) and a model Hamiltonian study to unravel the curious case of $NiRh_2O_4$, explaining existing data and making concrete predictions.

Density functional theory. We have carried out a first-principles study of $NiRh_2O_4$ in a full-potential all-electron approach of linear augmented plane wave method [34], muffin-tin orbital method [35,36], as well as in pseudopotential plane-wave basis [37] with projected augmented potential [38]. The exchange-correlation functional was chosen to

*arunp@physics.utoronto.ca

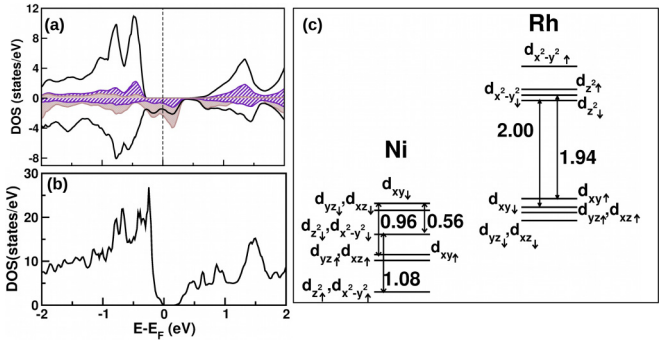

FIG. 1. (a) The GGA + U electronic structure of $NiRh_2O_4$ in low-temperature tetragonal phase. States projected onto Ni d, Rh d, and O p characters are shown as gray-shaded, black-solid line, and hatched areas, respectively. (b) The GGA + U + SOC electronic structure of $NiRh_2O_4$ in tetragonal phase. (c) The energy level positions for the spin-split and the crystal-field-split Ni d and Rh d states. For clarity, small splittings around 0.1 eV are not marked in the figure.

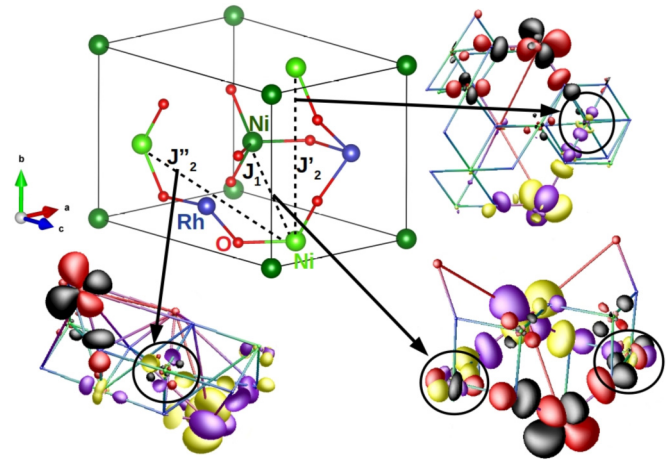

FIG. 2. The exchange pathways for first neighbor (J_1) and inequivalent second neighbors (J_2', J_2'') in the low-temperature tetragonal phase of $NiRh_2O_4$. Shown are the overlap of effective Ni Wannier functions placed at NN, in-plane NNN, and out-of-plane NNN Ni sites, with circles indicating nonzero weight at Rh sites in the pathway. Opposite sign parts of each Wannier function are colored differently.

be generalized gradient approximation (GGA) [39], supplemented with on-site Hubbard correction GGA + U [40]. Calculational details may be found in the Supplemental Material (SM) [41].

The electronic structure of $NiRh_2O_4$, within GGA + U ($U_{Ni} = 5$ eV, $J_H = 1$ eV), is half-metallic for both the high-temperature cubic and the low-temperature tetragonal phases. The spin splitting at the Ni site is large (≈1 eV) while that at the Rh site is an order of magnitude smaller (≈0.1 eV), in accordance with the nominal magnetic and nonmagnetic character of Ni^{2+} and Rh^{3+}, respectively. In the high-symmetry cubic phase (see SM [41] for details), the octahedral crystal field around Rh splits the 4d states into t_{2g} and e_g with a large splitting ∼3 eV, while the tetrahedral crystal field around Ni splits the 3d states into e and t_2 with a relatively smaller splitting ≈0.6 eV. The d states of high spin Ni are thus fully occupied in the up-spin channel; in the down-spin channel, the Ni t_2 states admixed with Rh t_{2g} and O p states cross the Fermi level (E_F). The Rh t_{2g} states are mostly occupied, except for the mixing with Ni states in the down-spin channel, while Rh e_g states are empty. This is in accordance with nominal valence of Ni^{2+} with two holes in t_2 manifold and low-spin d^6 occupancy of Rh. This general picture remains valid in the tetragonal phase as seen in Fig. 1. The tetragonal distortion, however, introduces additional splitting among the cubic symmetry split states. This splits the Ni t_2 states with Ni d_{xy} level positioned above Ni d_{xz}/d_{yz} with splitting of ≈0.1 eV. One of the two holes of Ni thus occupies the down-spin d_{xy} level, while the other hole occupies the down-spin doubly degenerate d_{xz}/d_{yz} levels. This leaves the GGA + U solution half-metallic even in the tetragonal phase, as shown in Fig. 1(a). The crystal and spin splittings in the tetragonal phase in Fig. 1(c) further highlight the energetic proximity of Ni t_2 and Rh t_{2g} states in the down-spin channel, driving a high degree of mixing between the two. This leads to a small magnetic moment ≈0.06–0.07μ_B at the otherwise nonmagnetic, low-spin, nominally d^6 Rh site, while the Ni moment is found to be 1.5–1.6μ_B. The remaining moment lives on O sites, giving rise to a net moment of 2μ_B/f.u. in both cubic and tetragonal phases.

Given the active Ni orbital degrees of freedom, we next explore the effect of SOC. Within the GGA + U + SOC approach, Ni supports partially occupied $d_{xz} \pm id_{yz}$ orbitals, with a large orbital moment of ∼1.0μ_B, leading to an $S = 1, L_{\text{eff}} = 1$ state, with parallel alignment of spin and orbital magnetization, in conformity with more than half-filled d occupancy of Ni. A GGA + SOC calculation leads to a significantly smaller estimate of Ni orbital moment of ≈0.1μ_B, due to the inability of GGA to capture the orbital polarization effect [42]. While GGA + SOC splits the partially occupied orbitally degenerate states in the down-spin channel, this is insufficient to open an insulating gap. This situation is similar to that of $FeCr_2S_4$ [43]. The Coulomb correlation within GGA + U + SOC is thus crucial for a renormalized, large, orbital polarization [44] and an ∼0.25 eV insulating charge gap [see Fig. 1(c)].

We next estimate the Ni-Ni magnetic exchange from the knowledge of the effective hopping strengths and on-site energies in the Wannier basis of Ni-t_2 only low-energy Hamiltonian (see SM for details). The dominant AFM interactions in cubic phase turn out to be between four nearest-neighbor (NN) Ni sites (J_1), which belong to two different face-centered cubic (fcc) sublattices of the diamond lattice, and 12 next-nearest neighbor (NNN) Ni sites (J_2), which belong to the same fcc sublattice. The tetragonal distortion splits the 12 NNN Ni-Ni interactions into four in-plane (J_2') and 8 out-of-plane (J_2'') interactions (see Fig. 2). The substantial mixing between Ni and Rh states, makes the Ni-O-Rh-O-Ni superexchange paths strong, as seen from the overlap of Wannier functions in Fig. 2 (see encircled part). The calculated exchanges are $J_1 \approx 1.2$ meV [45], with $J_2', J_2'' \approx 0.4J_1$, showing strong magnetic frustration. The scale of J_1 agrees with previous rough estimates [23].

Single-site model. Armed with the DFT results, we construct an effective single-site Hamiltonian for Ni^{2+} in the

tetrahedral crystal field. For two holes in the high-energy t_2 orbital, strong Hund's interaction favors total $L_{\rm eff} = 1$ and total $S = 1$. This orbital contribution was previously recognized [23]. The Hamiltonian including tetragonal distortion (δ) and SOC (λ) is

$$H = -\delta L_z^2 + \lambda \vec{L} \cdot \vec{S}, \tag{1}$$

where the sign of SOC arises from two holes in t_2 [46]. If $\lambda \gg \delta$, this leads to the $J_{\rm eff} = 0$ singlet ground state [30]. Here, based on DFT inputs, we consider $\delta \gg \lambda$, and show that this opposite limit leads to a simple, yet complete, understanding of the phenomenology of $NiRh_2O_4$.

In the regime $\delta \gg \lambda$, we start by constructing orbital eigenstates with well-defined L_z, which leads to a ground doublet with $L_z = \pm 1$ and an excited orbital singlet with $L_z = 0$ which is split off by a large energy δ. Next, let us take the spin degrees of freedom into account, which couple via SOC $\lambda \ll \delta$. The dominant SOC coupling is $\lambda L_z S_z$, which leads to a sequence of states in increasing order of energy which we label by $|L_z, S_z\rangle$:

$$\begin{aligned} &E_0^0\,[2] = -\delta - \lambda : |\pm, \mp\rangle; \quad E_1^0\,[2] = -\delta : |\pm, 0\rangle, \\ &E_2^0\,[2] = -\delta + \lambda : |\pm, \pm\rangle; \quad E_3^0\,[3] = 0 : |0, 0\rangle, |0, \pm\rangle \end{aligned} \tag{2}$$

with degeneracies shown in square brackets [46]. We can perturbatively treat $\lambda(L^+S^- + L^-S^+)/2$, since it only couples the low-lying states at $E^0_{0,1,2}$ to the high-energy states at E^0_3. Let us define the symmetric state $|e\rangle = (|+,-\rangle + |-,+\rangle)/\sqrt{2}$. We then find the sequence of states, with energies defined relative to the ground state,

$$\Delta_0 = 0 : |\psi_0\rangle \approx |e\rangle - \sqrt{2}\frac{\lambda}{\delta}|0,0\rangle, \tag{3}$$

$$\Delta_1 \approx 2\frac{\lambda^2}{\delta} : |\psi_1\rangle = \frac{|+,-\rangle - |-,+\rangle}{\sqrt{2}}, \tag{4}$$

$$\Delta_2 \approx \lambda + \frac{\lambda^2}{\delta} : |\psi_{2,\pm}\rangle \approx |\pm,0\rangle - \frac{\lambda}{\delta}|0,\pm\rangle, \tag{5}$$

$$\Delta_3 \approx 2\lambda + 2\frac{\lambda^2}{\delta} : |\psi_{3,\pm}\rangle = |\pm,\pm\rangle, \tag{6}$$

$$\Delta_4 \approx \delta + \lambda + 3\frac{\lambda^2}{\delta} : |\psi_{4\pm}\rangle \approx |0,\pm\rangle + \frac{\lambda}{\delta}|\pm,0\rangle, \tag{7}$$

$$\Delta_5 \approx \delta + \lambda + 4\frac{\lambda^2}{\delta} : |\psi_5\rangle \approx |0,0\rangle + \frac{\sqrt{2}\lambda}{\delta}|e\rangle. \tag{8}$$

With these states and energies in hand, and a choice $\lambda \sim 10$ meV and $\delta \sim 100$ meV, we readily obtain a broad-brush understanding of some key experimental observations as summarized below. (The choice of $\delta \sim 100$ meV agrees with the spin-averaged crystal field splitting between d_{xy} and d_{yz}/d_{xz} orbitals from our DFT). We present further arguments against alternative scenarios in the SM [41].

Ground state. We find that the ground state is a nonmagnetic singlet. This is consistent with the lack of any magnetic order down to the lowest temperature in this material [47]. In contrast to previous work, our proposed nonmagnetic ground state is a spin-orbit entangled "Schrödinger-cat" type singlet state, arising from weak splitting of a doublet due to off-diagonal SOC.

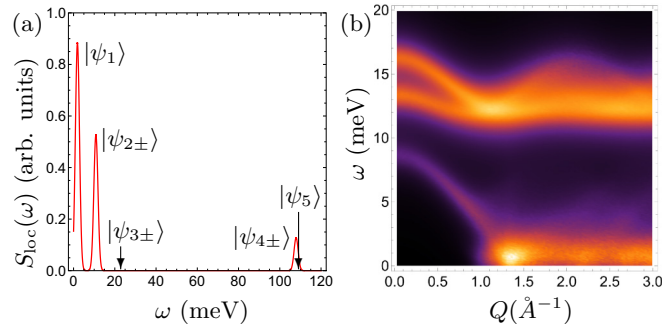

FIG. 3. (a) Local dynamical spin correlation function $S_{\rm loc}(\omega)$ within single-site model. Peaks are labeled by relevant excited states, and arrows indicate "dark states" invisible to neutrons due to vanishing matrix elements. (b) Intensity plot (arbitrary units) of powder-averaged INS spin structure factor, $\mathcal{S}(Q,\omega)$, as a function of wave vector Q and energy ω (with 1 meV broadening to mimic experimental resolution); see text for details.

Thermodynamics. Since the gap to the states $|\psi_{4\pm}\rangle, |\psi_5\rangle$ is large, we recover only an entropy $S_{\rm low} = R \ln 6$ for $T < 300$ K, consistent with previous work [23] and specific heat up to room temperature (i.e., for $T \ll \Delta_4$). At low T, Δ_1 leads to a Schottky peak in C/T at $T \sim 10$ K from the level $|\psi_1\rangle$ (see SM [41]). It is not clear why this peak has not been observed; it may be smeared by defects which likely lead to the observed spin freezing for $T \lesssim 6$ K. The higher levels $|\psi_{2\pm}\rangle$ lead to a broad Schottky peak at $T \sim 40$ K, as observed.

Neutron scattering. Our results for the local dynamical spin correlation function $S_{\rm loc}(\omega)$ are summarized in Fig. 3(a). The first excited state is nondegenerate, separated by an energy $\Delta_1 \approx 2\lambda^2/\Delta \approx 2$ meV. We note that $|\psi_0\rangle$ and $|\psi_1\rangle$ are connected via S^z, so $|\psi_1\rangle$ should be visible in non-spin-flip scattering, but appears difficult to observe due to the resolution and the background, as well as possibly defects. The second excited state is a doublet $|\psi_{2,\pm}\rangle$ with an energy gap $\Delta_2 \approx \lambda + \lambda^2/\Delta$. We propose that it is this doublet state which has been observed as a gapped mode in INS experiments [23]. The above parameter choice leads to the gap $\Delta_2 \approx 11$ meV, in crude agreement with the data. Based on our analysis, the states $|\psi_{3\pm}\rangle$ at an energy gap $\Delta_3 \approx 22$ meV and the singlet state $|\psi_5\rangle$ at a gap $\Delta_4 \approx 108$ meV are both "dark states," invisible to neutrons due to vanishing matrix elements. Finally, $|\psi_{4\pm}\rangle$ with a gap $\Delta_5 \approx 107$ meV should be visible but with spectral weight much smaller that of $|\psi_{2\pm}\rangle$. This is a prediction for future INS experiments.

Magnetic susceptibility. The computed single-site magnetic susceptibility χ can be fit to an apparent "Curie-Weiss" form $\chi(T) = \chi_0 + \alpha/(T - T_0)$, with a negligible background $\chi_0 \sim 10^{-5}$, an effective "Curie-Weiss" scale $T_0 \approx 16(2)$ K, and $\alpha \approx 0.85(2)$ (see SM) [48]. In analyzing experiments, we expect χ_0 will get lumped together with a background van Vleck type contribution which is conventionally subtracted. Our estimate for T_0 is small and "ferromagnetic" in sign, so that the $T_0^{\rm expt.} \approx -11$ K observed in experiments [23] must be attributed to weak residual intersite AFM exchanges $\sim$1 meV. Setting the fitted $\alpha \equiv S_{\rm eff}(S_{\rm eff}+1)/3$, yields an effective spin $S_{\rm eff} = 1.4$ (or an effective magnetic moment $p_{\rm eff} \sim 3.6\mu_B$), larger than a spin-only value $S = 1$ [23].

Intersite exchange. We next incorporate intersite interactions via a simple J_1-J_2 Heisenberg exchange model $H_{\rm ex} = \frac{1}{2}\sum_{i,j} J_{ij}\mathbf{S}_i \cdot \mathbf{S}_j$. In order to compute the spin dynamics in the low-energy Hilbert space, we introduce, in the spirit of slave-boson theory [30,49,50], four local boson operators, $c_0^\dagger$, $c_1^\dagger$, $d_\pm^\dagger$, which respectively create states $|\psi_0\rangle$, $|\psi_1\rangle$, and $|\psi_{2\pm}\rangle$. Projecting the Heisenberg model to this Hilbert subspace, and imposing the local completeness constraint $c_0^\dagger c_0 + c_1^\dagger c_1 + d_\alpha^\dagger d_\alpha = 1$ (with an implicit sum on $\alpha = \pm$), we find that the site spin-1 operators may be approximated as $S^z = (c_1^\dagger c_0 + c_0^\dagger c_1)$ and $S^\pm = (c_0^\dagger \pm c_1^\dagger)d_\pm + d_\mp^\dagger(c_0 \mp c_1)$. At mean-field level, we replace $c_0 \to \langle c_0\rangle$, and retain leading powers in $\langle c_0\rangle$, to arrive at the Hamiltonian $H_{\rm tot} = H_{\rm loc} + H_{\rm ex} + H_{\rm con}$, where

$$H_{\rm loc} = \sum_i (\Delta_1 c_{i1}^\dagger c_{i1} + \Delta_2 d_{i\alpha}^\dagger d_{i\alpha}), \tag{9}$$

$$H_{\rm ex} = \frac{1}{4}\langle c_0\rangle^2 \sum_{i,j} J_{ij}[(d_{i\alpha}^\dagger d_{j\alpha} + d_{i\alpha}^\dagger d_{j\bar{\alpha}}^\dagger + \text{H.c.}) + 2(c_{i1}^\dagger + c_{i1})(c_{j1}^\dagger + c_{j1})], \tag{10}$$

$$H_{\rm con} = -\mu \sum_i (c_{i1}^\dagger c_{i1} + d_{i\alpha}^\dagger d_{i\alpha} + \langle c_0\rangle^2 - 1). \tag{11}$$

Fluctuations are not expected to qualitatively impact our results. The different pieces correspond respectively to the local single-site Hamiltonian, the intersite exchange Hamiltonian, and the constraint imposed (on average) via the Lagrange multiplier μ. We note that the c and d bosons are decoupled at this order (except for the constraint). We can thus solve this in momentum space separately for these two sectors, leading to

$$H_{\rm tot} = \sum_{\mathbf{k},\sigma} \left(E_{\mathbf{k}}^\sigma \alpha_{\mathbf{k},\sigma}^\dagger \alpha_{\mathbf{k},\sigma} + \tilde{E}_{\mathbf{k}}^\sigma \beta_{\mathbf{k},\sigma}^\dagger \beta_{\mathbf{k},\sigma}\right) - 2\mu \sum_{\mathbf{k}} \langle c_0\rangle^2 + \sum_{\mathbf{k}\sigma}\left(\frac{1}{2}E_{\mathbf{k}}^\sigma + \tilde{E}_{\mathbf{k}}^\sigma\right) - \sum_{\mathbf{k}}(\Delta_1 + 2\Delta_2 - 5\mu). \tag{12}$$

Here, $\sigma = \pm$, and the excitation energies are given by

$$E_{\mathbf{k}}^\sigma = (\Delta_1 - \mu)^{1/2}[\Delta_1 - \mu + 2\langle c_0\rangle^2(\sigma J_1|\gamma_{\mathbf{k}}| + J_2\eta_{\mathbf{k}})]^{1/2}, \tag{13}$$

$$\tilde{E}_{\mathbf{k}}^\sigma = (\Delta_2 - \mu)^{1/2}[\Delta_2 - \mu + \langle c_0\rangle^2(\sigma J_1|\gamma_{\mathbf{k}}| + J_2\eta_{\mathbf{k}})]^{1/2} \tag{14}$$

with $\gamma_{\mathbf{k}} = \sum_{\ell_1} e^{i\mathbf{k}\cdot\ell_1}$ and $\eta_{\mathbf{k}} = \sum_{\ell_2} e^{i\mathbf{k}\cdot\ell_2}$, where ℓ_1, ℓ_2 are respectively the 4 nearest-neighbor and 12 next-neighbor vectors. We choose $\Delta_1 = 1.8$ meV and $\Delta_2 = 11$ meV from the single-site model, and $J_1 = 1.2$ meV and $J_2/J_1 = 0.4$ from DFT. Using these, we minimize the ground-state energy with respect to $\langle c_0\rangle^2$, choosing μ to satisfy the constraint. We find the optimal $\langle c_0\rangle^2 \approx 0.7$ and $\mu \approx -2.1$ meV.

The resulting weighted and powder-averaged dynamic spin structure factor relevant to INS experiments, $\mathcal{S}(\mathbf{Q},\omega) = \sum_\alpha (1 - Q_\alpha^2/Q^2) S_{\alpha\alpha}(\mathbf{Q},\omega)$, including a 1 meV broadening to mimic the experimental resolution but ignoring form factors, is plotted in Fig. 3(b) (see also SM [41]). The upper gapped mode, arising from the $|\psi_{2\pm}\rangle$ states, is in rough agreement with INS observations of a gapped dispersive mode [23]; we find that it really consists of two peaks due to two sublattices on the diamond lattice. The lower gapped mode is the "optical branch" of the $|\psi_1\rangle$ state. It collapses in energy, with increasing Q, from ~8 meV down to ~0.5 meV, and persists as an intense small-gap band, robust against magnetic condensate formation due to frustrating J_2 exchange. The lower-energy "acoustic branch" of the $|\psi_1\rangle$ state is also gapped, but it has negligible intensity and is not visible here (see SM [41]). The small-Q behavior depicted here may be partly masked by neutron kinematic constraints.

Summary and discussion. We have combined DFT and model calculations to address the mystery of $NiRh_2O_4$, broadly capturing the existing thermodynamic and INS observations. In light of our work, it may be useful to revisit the low-temperature specific heat and low-energy INS on higher purity samples, and use INS to probe the predicted high-energy crystal field level around ~110 meV. Terahertz spectroscopy [51,52] on $NiRh_2O_4$ could help to test our prediction of the "optical" $|\psi_1\rangle$ mode at $Q = 0$. It may be possible to use Raman or resonant inelastic x-ray scattering at a Ni edge [53] to look for the predicted $|\psi_{3\pm}\rangle$ and $|\psi_5\rangle$ "dark states" which are invisible to neutrons. Finally, our work shows that $NiRh_2O_4$ does not realize a topological quantum paramagnet. However, it guides future searches by suggesting that tetragonal compression, presumably achievable by application of uniaxial strain, may provide the means to quench orbital angular momentum and suppress SOC effects, potentially stabilizing more exotic phases.

Acknowledgments. A.P. was supported by NSERC of Canada. T.S.-D. thanks the Department of Science and Technology, India for the support through a Thematic Unit of Excellence.

[1] M. Z. Hasan and C. L. Kane, Rev. Mod. Phys. **82**, 3045 (2010).
[2] X.-L. Qi and S.-C. Zhang, Rev. Mod. Phys. **83**, 1057 (2011).
[3] B. Yan and C. Felser, Annu. Rev. Condens. Matter Phys. **8**, 337 (2017).
[4] A. Vishwanath and T. Senthil, Phys. Rev. X **3**, 011016 (2013).
[5] M. Levin and Z.-C. Gu, Phys. Rev. B **86**, 115109 (2012).
[6] F. Pollmann, E. Berg, A. M. Turner, and M. Oshikawa, Phys. Rev. B **85**, 075125 (2012).
[7] T. Senthil and M. Levin, Phys. Rev. Lett. **110**, 046801 (2013).
[8] T. Senthil, Annu. Rev. Condens. Matter Phys. **6**, 299 (2015).
[9] C. Wang, A. Nahum, and T. Senthil, Phys. Rev. B **91**, 195131 (2015).
[10] F. D. M. Haldane, Phys. Rev. Lett. **50**, 1153 (1983).
[11] I. Affleck, T. Kennedy, E. H. Lieb, and H. Tasaki, Phys. Rev. Lett. **59**, 799 (1987).
[12] V. Fritsch, J. Hemberger, N. Büttgen, E.-W. Scheidt, H.-A. Krug von Nidda, A. Loidl, and V. Tsurkan, Phys. Rev. Lett. **92**, 116401 (2004).
[13] N. Tristan, J. Hemberger, A. Krimmel, H.-A. Krug von Nidda, V. Tsurkan, and A. Loidl, Phys. Rev. B **72**, 174404 (2005).

[14] D. Bergman, J. Alicea, E. Gull, S. Trebst, and L. Balents, Nat. Phys. **3**, 487 (2007).

[15] J.-S. Bernier, M. J. Lawler, and Y. B. Kim, Phys. Rev. Lett. **101**, 047201 (2008).

[16] S. Gao, O. Zaharko, V. Tsurkan, Y. Su, J. S. White, G. S. Tucker, B. Roessli, F. Bourdarot, R. Sibille, D. Chernyshov *et al.*, Nat. Phys. **13**, 157 (2016).

[17] L. Ge, J. Flynn, J. A. M. Paddison, M. B. Stone, S. Calder, M. A. Subramanian, A. P. Ramirez, and M. Mourigal, Phys. Rev. B **96**, 064413 (2017).

[18] J. Oitmaa, Phys. Rev. B **99**, 134407 (2019).

[19] G. Chen, L. Balents, and A. P. Schnyder, Phys. Rev. Lett. **102**, 096406 (2009).

[20] G. Chen, A. P. Schnyder, and L. Balents, Phys. Rev. B **80**, 224409 (2009).

[21] K. W. Plumb, J. R. Morey, J. A. Rodriguez-Rivera, H. Wu, A. A. Podlesnyak, T. M. McQueen, and C. L. Broholm, Phys. Rev. X **6**, 041055 (2016).

[22] V. Tsurkan, L. Prodan, V. Felea, I. Filippova, V. Kravtsov, A. Günther, S. Widmann, H.-A. Krug von Nidda, J. Deisenhofer, and A. Loidl, Phys. Rev. B **96**, 054417 (2017).

[23] J. R. Chamorro, L. Ge, J. Flynn, M. A. Subramanian, M. Mourigal, and T. M. McQueen, Phys. Rev. Mater. **2**, 034404 (2018).

[24] G. Blasse and D. Schipper, Phys. Lett. **5**, 300 (1963).

[25] O. Tchernyshyov, Phys. Rev. Lett. **93**, 157206 (2004).

[26] T. Maitra and R. Valenti, Phys. Rev. Lett. **99**, 126401 (2007).

[27] The calculations in our Rapid Communication show that the correct crystal-field-level scheme is different; e.g., in the large distortion limit, Ref. [23] has a singlet Γ_1 ground state with a triplet excited Γ_5 state, while we predict a weakly split doublet ground state with a further excited doublet at the SOC scale $\sim\lambda$.

[28] G. Chen, Phys. Rev. B **96**, 020412(R) (2017).

[29] F. L. Buessen, M. Hering, J. Reuther, and S. Trebst, Phys. Rev. Lett. **120**, 057201 (2018).

[30] F.-Y. Li and G. Chen, Phys. Rev. B **100**, 045103 (2019).

[31] G. Khaliullin, Phys. Rev. Lett. **111**, 197201 (2013).

[32] A. Akbari and G. Khaliullin, Phys. Rev. B **90**, 035137 (2014).

[33] C. Svoboda, M. Randeria, and N. Trivedi, Phys. Rev. B **95**, 014409 (2017).

[34] P. Blaha, K. Schwarz, G. K. H. Masden, D. Kvasnicka, and J. Luitz, *Wien2k, An Augumented Plane Wave+Local Orbitals Program for Calculating Crystal Properties* (Technische Universitiät Wien, Vienna, 2001).

[35] O. K. Andersen and O. Jepsen, Phys. Rev. Lett. **53**, 2571 (1984).

[36] O. K. Andersen and T. Saha-Dasgupta, Phys. Rev. B **62**, R16219(R) (2000).

[37] G. Kresse and J. Furthmüller, Phys. Rev. B **54**, 11169 (1996).

[38] P. E. Blöchl, Phys. Rev. B **50**, 17953 (1994).

[39] J. P. Perdew, K. Burke, and M. Ernzerhof, Phys. Rev. Lett. **77**, 3865 (1996).

[40] V. I. Anisimov, I. V. Solovyev, M. A. Korotin, M. T. Czyżyk, and G. A. Sawatzky, Phys. Rev. B **48**, 16929 (1993).

[41] See Supplemental Material at http://link.aps.org/supplemental/10.1103/PhysRevB.100.140408 which gives (i) details of crystal structure, (ii) details of calculational methods used in DFT, (iii) plots of single-site magnetic entropy, specific heat, and magnetic susceptibility, (iv) further arguments in favor of the scenario discussed in the Rapid Communication, and (v) plot of powder-averaged spectrum.

[42] The calculated orbital moment at the Rh site is found to be smaller than that of Ni ($\approx 0.05\mu_B$) both within GGA+SOC and GGA+U+SOC, suggesting near quenching of orbital moment at the Rh site.

[43] S. Sarkar, M. De Raychaudhury, I. Dasgupta, and T. Saha-Dasgupta, Phys. Rev. B **80**, 201101(R) (2009).

[44] The calculated spin-ion anisotropy in the cubic phase is $\approx$10 meV per Ni ion with easy axis along the (111) direction.

[45] Varying the U_{Ni} value between 5 and 7 eV, the dominant interaction J_1 is found to vary between 1.2 and 0.8 meV, with little changes in the ratios of magnetic exchanges.

[46] As is well known, projecting to the t_2 manifold flips the sign of the orbital angular momentum, so $L_{\mathrm{eff}} = 1$ carries an orbital magnetic moment $\propto(-\vec{L})$. Thus, the state $|L_z, S_z\rangle = |+, -\rangle$ has orbital and spin magnetic moments which are actually parallel, exactly as in the full DFT.

[47] This point appears to have been clearly appreciated by the authors of Ref. [23].

[48] The uncertainties in these estimates arise from varying the range of the fit.

[49] S. Sachdev and R. N. Bhatt, Phys. Rev. B **41**, 9323 (1990).

[50] F.-Y. Li and G. Chen, Phys. Rev. B **98**, 045109 (2018).

[51] N. J. Laurita, J. Deisenhofer, L. D. Pan, C. M. Morris, M. Schmidt, M. Johnsson, V. Tsurkan, A. Loidl, and N. P. Armitage, Phys. Rev. Lett. **114**, 207201 (2015).

[52] X. Zhang, F. Mahmood, M. Daum, Z. Dun, J. A. M. Paddison, N. J. Laurita, T. Hong, H. Zhou, N. P. Armitage, and M. Mourigal, Phys. Rev. X **8**, 031001 (2018).

[53] Y. Lu, D. Betto, K. Fürsich, H. Suzuki, H.-H. Kim, G. Cristiani, G. Logvenov, N. B. Brookes, E. Benckiser, M. W. Haverkort *et al.*, Phys. Rev. X **8**, 031014 (2018).